Science & Technology Development Journal 2024, ():1-13

Open Access Full Text Article

Research Article

Evaluation of the forming quality of Inconel 625 thin-walled parts manufactured via cold metal transfer additive manufacturing

Duc Manh Dinh[1], Hoang Son Lam[2], Van Thao Le[1,*], Quoc Hoang Pham[1]

ABSTRACT

Introduction: Wire arc additive manufacturing (WAAM) is a metal additive manufacturing technique that uses an arc source to melt metallic wires, depositing molten metal layer by layer to form parts. Controlling the forming quality of parts in the WAAM process poses significant challenges. This study evaluated the shape quality of thin walls produced via WAAM using Inconel 625 alloy. Additionally, the impacts of the welding speed (v) and linear heat input (LHI) on the geometric quality of the fabricated components are investigated.

Methods: A cold metal transfer (CMT)-WAAM system was employed to construct thin-walled samples on low-carbon substrates. Three samples were fabricated at three different welding speeds (*v* = 35, 50, and 65 cm/min), while the other parameters remained constant. The samples were scanned via a Kreon Zypher II scanner, and their geometric properties, including average layer height (*ALH*), total wall width (*TW*), effective wall width (*EW*), and material deposition efficiency (*DE*), were measured via Geomagic Design X and AutoCAD software. Surface roughness parameters (e.g., S_z, S_a, and S_q) were assessed via Omnisurf 3D software.

Results and Discussion: Increasing the welding speed from 35 to 65 cm/min led to reductions in all measured characteristics - *ALH*, *TW*, *EW*, and *DE*. For example, *ALH* decreases from 2.63 mm to 1.87 mm, *TW* decreases from 9.39 mm to 6.83 mm, and *EW* decreases from 5.90 mm to 4.30 mm. An increase in the *LHI* from 19.08 to 35.22 J/mm tends to inversely affect these geometric characteristics. Additionally, as *v* or *LHI* increases, S_z, S_a, and S_q initially decrease to a certain level before rising again.

Conclusions: The results obtained from this study offer valuable insights into the relationship between processing and forming quality in the CMT-WAAM process for Inconel 625 thin-wall components. These insights provide a foundation for selecting optimal process parameters and providing informed recommendations for the CMT-WAAM process of Inconel 625 alloys.

Key words: Additive manufacturing, Wire arc additive manufacturing, Cold metal transfer, Forming quality, Inconel 625

[1]*Advanced Technology Center, Le Quy Don Technical University*

[2]*Mechanical Electrical Engineering 151 Co., Ltd.*

Correspondence

Van Thao Le, Advanced Technology Center, Le Quy Don Technical University

Email: thaomta@gmail.com

History

- Received: 2024-05-08
- Revised: 2024-08-15
- Accepted: 2024-08-17
- Published Online:

DOI :

INTRODUCTION

WAAM technology is a 3D printing technology that uses a metal welding wire as the input material [1–3]. The arc energy sources used in the WAAM process can include gas metal arc welding (GMAW or MIG), cold metal transfer (CMT), gas tungsten arc welding (GTAW or TIG), and plasma arc welding (PAW) [4]. Compared with other additive manufacturing (AM) technologies that use laser or electron beam sources and metal powder (e.g., from 0.1 to 0.6 kg/h), WAAM has a superior material deposition rate (from 3 to 8 kg/h) [5,6]. Moreover, requirements for the environment are not too strict, making this technology capable of manufacturing large parts. The WAAM system also has lower investmentcosts [7]. Currently, WAAM plays a very important role in many fields, such as the aerospace, construction, structural, nuclear energy, and marine industries [8–13].

Many studies on the WAAM process for various alloys (e.g., steels, aluminum, titanium, and nickel-based alloys) have been reported in the literature. These studies have focused mostly on the effects of WAAM parameters on microstructures and mechanical properties [14–17]. However, research evaluating the influence of process parameters on the geometric shape and surface roughness of a product is limited to only certain types of materials, such as stainless steel and low-carbon steel. For example, Dinovitzer et al. [18] reported that when the welding speed increased, the surface roughness increased, and an inverse relationship was observed between the current applied during the WAAM process of the HASTELLOY X alloy. Xiong et al. [19] provided a quantitative evaluation approach for the surface roughness of thin-walled parts.

Inconel 625 is known as a nickel-based superalloy with high strength and good heat, corrosion, and

Cite this article : Dinh D M, Lam H S, Le V T, Pham Q H. **Evaluation of the forming quality of Inconel 625 thin-walled parts manufactured via cold metal transfer additive manufacturing**. *Sci. Tech. Dev. J.* 2024; ():1-13.

oxidation resistance. This alloy has a high bearing capacity and a wide temperature range, from cryogenic temperatures to 982°C [14,15]. Several studies have been published on the microstructures, mechanical properties, corrosion resistance, residual stress, and defects of WAAMed Inconel 625 parts. Xu et al. [20] investigated the microstructures and mechanical properties of Inconel 625 parts fabricated by PAW-WAAMed with a continuous deposition strategy (CDS) and an interpass cooling strategy (ICS). They reported that the fabricated parts revealed columnar dendrite structures decorated with a large amount of Laves phase (MC carbides and Ni3Nb), and ICS improved the mechanical properties and surface quality compared with those of CDS. Cheepu et al. [21] examined the effects of different deposition strategies for Inconel 625 alloys via super-TIG-WAAM. They reported that multi-pass beads with stringer and zigzag layering strategies could refine microstructures. Recently, Kumar et al. [22] performed a parametric study and optimization of weld beads in GMAW-WAAM of Inconel 625 via the RSM and DA methods. Motwani et al. [23] presented a study on multi-response optimization in CMT-WAAM of Inconel 625 via entropy weightage-assisted gray-based Taguchi analysis.

Until recently, the influence of process parameters on the geometric characteristics of Inconel 625 products built via WAAM has rarely been reported. Therefore, this work aims to analyze the geometric characteristics of Inconel 625 thin-walled parts produced via CMT-WAAM technology and examine the effects of the welding speed (v) and linear heat input (LHI) on the part-forming quality. LHI refers to the amount of heat applied per unit length of weld track. In WAAM, LHI is the parameter with the greatest impact on the cooling rate that drives the shaping quality, microstructures, and mechanical properties, whereas v is strongly related to the part geometry and productivity. In the present study, we aimed to evaluate the geometric characteristics of the as-built part, including the average layer height (ALH), total width (TW), effective width (EW), and surface roughness of the thin-walled parts and the deposition efficiency (DE), and the effects of v and LHI on these characteristics. The outcomes enable us to discuss the actual process parameter selection for manufacturing Inconel 625 components with CMT-WAAM technology.

The structure of this article is as follows: The materials and experimental procedures are described in section 2. The primary findings regarding the geometric properties and surface roughness of the building materials are provided in the Results and Discussion section. The last section, conclusions, provides an overview of significant findings and suggestions for the future.

MATERIALS AND METHODS

Materials

In this research, DAIKO SF 625 welding wire, which has a broad operating temperature range from -269°C to 1000°C, was used. Its diameter is 1.2 mm, and the chemical composition of the wire is presented in Table 1 (according to the AWS A5.14 standard):

The material used in the experimental process was S45C (JIS G4051) steel. The chemical composition of the substrate included 0.48 C, 0.35 Si, 0.9 Mn, 0.03 P, 0.035 S, 0.2 Ni, 0.2 Cr, and 0.3 Cu (in wt.%). Its dimensions are 200 mm × 200 mm × 10 mm in length, width, and height, respectively. On the other hand, the plate was cleaned before the experiment.

CMT-WAAM system

All the samples were fabricated on the CMT-WAAM system, as shown in Figure 1. It consists of a CMT welding unit (TPS 320i) and a 6-axis robot (FD-V8 OTC Daihen). During welding, the motion of the welding wire is regulated with an average frequency of approximately 70 Hz [24–27], and the power source is supplied intermittently during each short-circuit period to create the arc and melt the metal wire. As a result, molten metal droplets were steadily controlled into the welding pool.

With the CMT welding principle, the welding wire is first moved closer to the substrate to start the welding process. An arc is formed, and the welding head is controlled to process the molten metal into the welding pool by moving the welding wire closer and farther away to minimize the thermal effect in the welding area. At the end of a welding line, the process is repeated. The weld beads are built on each other until the part is completed.

Building thin-walled samples and data collection methods

In this study, three rectangular thin-walled samples were subjected to three different welding speeds (v = 65, 50, and 35 cm/min), and the wire feed speed (WFS) was held constant at 6.5 m/min, as shown in Table 2. The linear heat input (LHI) is calculated according to Eq. (1).

$$LHI = \eta \times \frac{U \times I}{v} \, (J/mm)$$

where η is the energy conversion efficiency (normally, η = 85% for CMT), and U and I are the voltage and

Table 1: Chemical composition of the welding wire (in wt.%)

C	Mn	Si	S	P	Cr	Ni	Mo	Nb+Ta	Cu	Al	Ti	Fe
0.02	0.02	0.1	0.005	0.005	22	65	9	3.5	0.05	0.2	0.2	<0.5

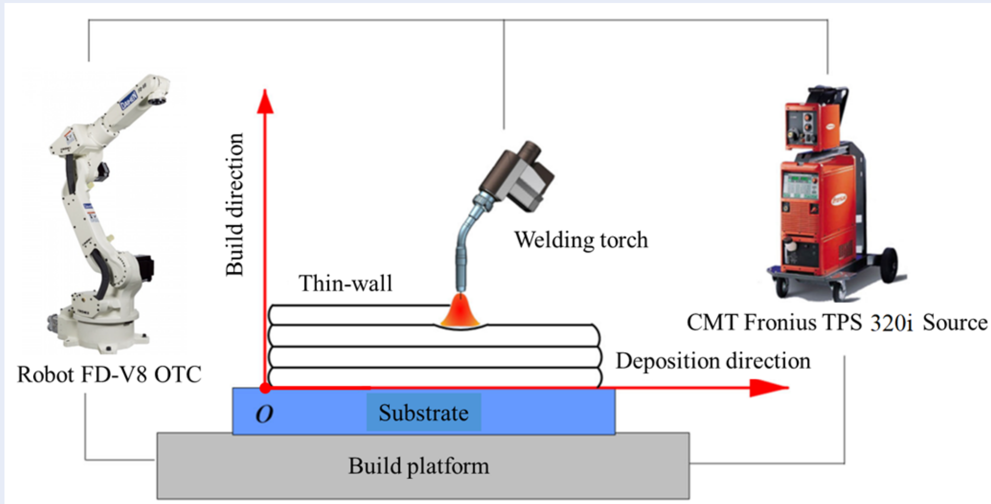

Figure 1: CMT-WAAM system used for building thin-walled parts

current, respectively. With the CMT power source, U and I were automatically set according to the value of the wire feed speed, as shown in Table 2.

The thin-walled samples were made of 20 layers, and the programmed dimension of each layer was the same, with dimensions of 130 mm in length and 60 mm in width. The starting point, the ending point, and the transfer point between the layers are the same and are in the middle of the length dimension. During the deposition process, the arc was emitted continuously according to the CMT principle. Moreover, commercially pure argon was used (99.99% Ar) with a flow rate of 16 $L.min^{-1}$ to protect the welding pool. All the samples were fabricated at room temperature. The distance between the torch tip and the workpiece surface was fixed at 10 mm. The angle between the axis of the welding torch and the substrate was also maintained at 90 degrees.

After fabrication, all the samples were scanned by a Kreon Zypher II scanner to collect their actual shape. The scanned data were then processed with Geomagic Design X software, as shown in Figure 2.

In this study, the geometric characteristics of the thin walls investigated are illustrated in Figure 3, including the total width (TW), the effective width (EW), the total height (TH), and the effective wall height (EH). The average layer height (ALH) is determined by the ratio between TH and the number of printed layers.

The method used to analyze the geometrical characteristics is presented in Figure 4. Each thin-walled sample was evaluated at four cross-sections (cs1, cs2, cs3, and cs4). The distance between two adjacent cross-sections is 25 mm. cs1 and cs2 are symmetrical with respect to cs4 and cs3, respectively, through the center plane along the length of the scanned sample. This ensures the survey along the entire length of the deposition path and monitoring the difference in profile at the beginning and end of the deposition line. These intersection profiles were processed in AutoCAD software to measure ALH, TW, EW, and DE.

The material deposition efficiency (DE) is a value that represents the efficiency of the entire WAAM process in general. It is determined by the ratio of the effective cross-sectional area to the total cross-sectional area at the local location under consideration, as described in Eq. (2), where the effective cross-sectional area is calculated via the values of effective width (EW) and effective height (EH).

$$DE = \frac{EH \times EW}{Total\ area} \tag{2}$$

The process for evaluating the surface roughness parameters is shown in Figure 5. For each sample, two portions of the opposite surface on each wall along the length of the sample were cut. Each portion has the same dimensions of 70 mm × 30 mm. These four

Table 2: **Setup input and actual process parameters**

No.	Number of layers	Target		Actual		
		WFS (m/min)	v (cm/min)	I (A)	U (V)	LHI (J/mm)
1	20	6.5	65	160	15.2	191
2	20	6.5	50	157	15.3	245
3	20	6.5	35	158	15.3	352

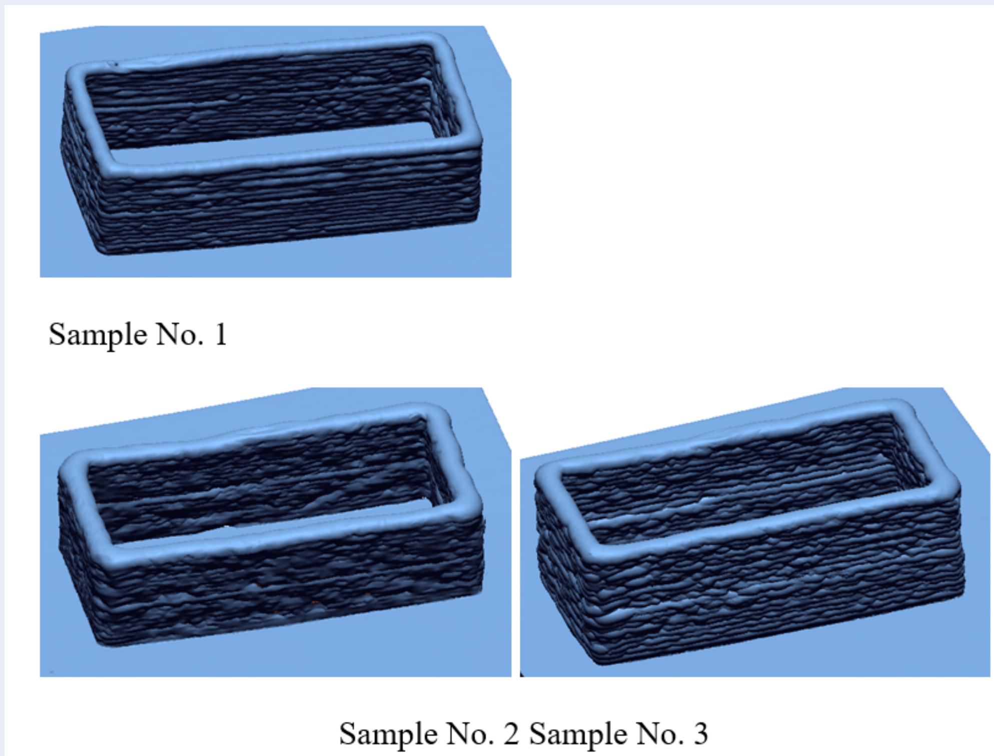

Figure 2: 3D scanned data of the samples

surface samples were subsequently used to analyze the surface roughness parameters via Omnisurf 3D software. The studied roughness parameters are the maximum roughness S_z, average roughness S_a, and mean square roughness S_q, which are calculated via Eqs. (3), (4), and (5), respectively.

$$S_z = z_{max}(x,y) - z_{min}(x,y) \quad (3)$$

$$S_a = \frac{1}{S}\int\int_s |z(x,y)|\,dxdy \quad (4)$$

$$S_q = \sqrt{\frac{1}{S}\int\int_s z^2(x,y)\,dxdy} \quad (5)$$

where *z(x,y)* represents the coordinates of the grid points and   represents the surface area.

RESULTS

Geometric characteristics

The results regarding the geometric characteristics (including *TW*, *TH*, *EW*, *EH*, and *ALH*) of the thin-wall samples fabricated via CMT-WAAM are displayed in Tables 3 and 4, respectively. For each type of output result, the average values from the measurements were calculated to construct graphs.

The graphs that depict the influence of the welding speed *v* on *ALH*, *TW*, and *EW* are presented in Figure 6. The *ALH* decreases proportionally with the welding speed *v*. The *ALH* decreases from 2.63 mm to 1.83 mm when *v* increases from 35 cm/min to 65 cm/min. *ALH* tends to decrease rapidly at lower

Table 3: Obtained geometric parameters

Sample	Cross section	Obtained data			
		TW (mm)	TH (mm)	EW (mm)	EH (mm)
No.1	cs1	6.87	36.49	4.39	35.05
		7.2	37.25	4.42	35.25
	cs2	6.58	36.89	4.37	35.51
		6.97	38.47	4.06	37.03
	cs3	6.79	37.18	4.22	35.64
		6.81	38.04	3.98	36.74
	cs4	6.7	36.83	4.67	35.03
		6.75	37.26	4.31	35.79
	Average	6.83	37.30	4.30	35.76
	Standard deviation	± 0.19	± 0.65	± 0.22	± 0.75
No. 2	cs1	8.06	41.13	5.22	39.28
		7,67	40.95	4.81	39.09
	cs2	7.99	41.18	5.27	39.94
		7.94	41.34	4.98	40.37
	cs3	8.43	40.48	5.52	38.45
		7.90	40.67	4.54	38.68
	cs4	8.18	40.76	5.34	39.13
		7.86	40.89	4.64	39.18
	Average	8.00	40.93	5.04	39.27
	Standard deviation	± 0.23	± 0.29	± 0.35	± 0.63
No. 3	cs1	9.32	52.57	5.62	51.7
		9.98	51.86	5.82	50.77
	cs2	9.04	52.54	6.02	51.19
		9.51	52.27	5.78	50.95
	cs3	9.24	52.76	6.15	51.51
		9.6	52.79	5.89	51.42
	cs4	9.22	52.73	5.56	51.49
		9.21	52.6	6.33	51.19
	Average	9.39	52.52	5.90	51.28
	Standard deviation	± 0.30	± 0.31	± 0.26	± 0.31

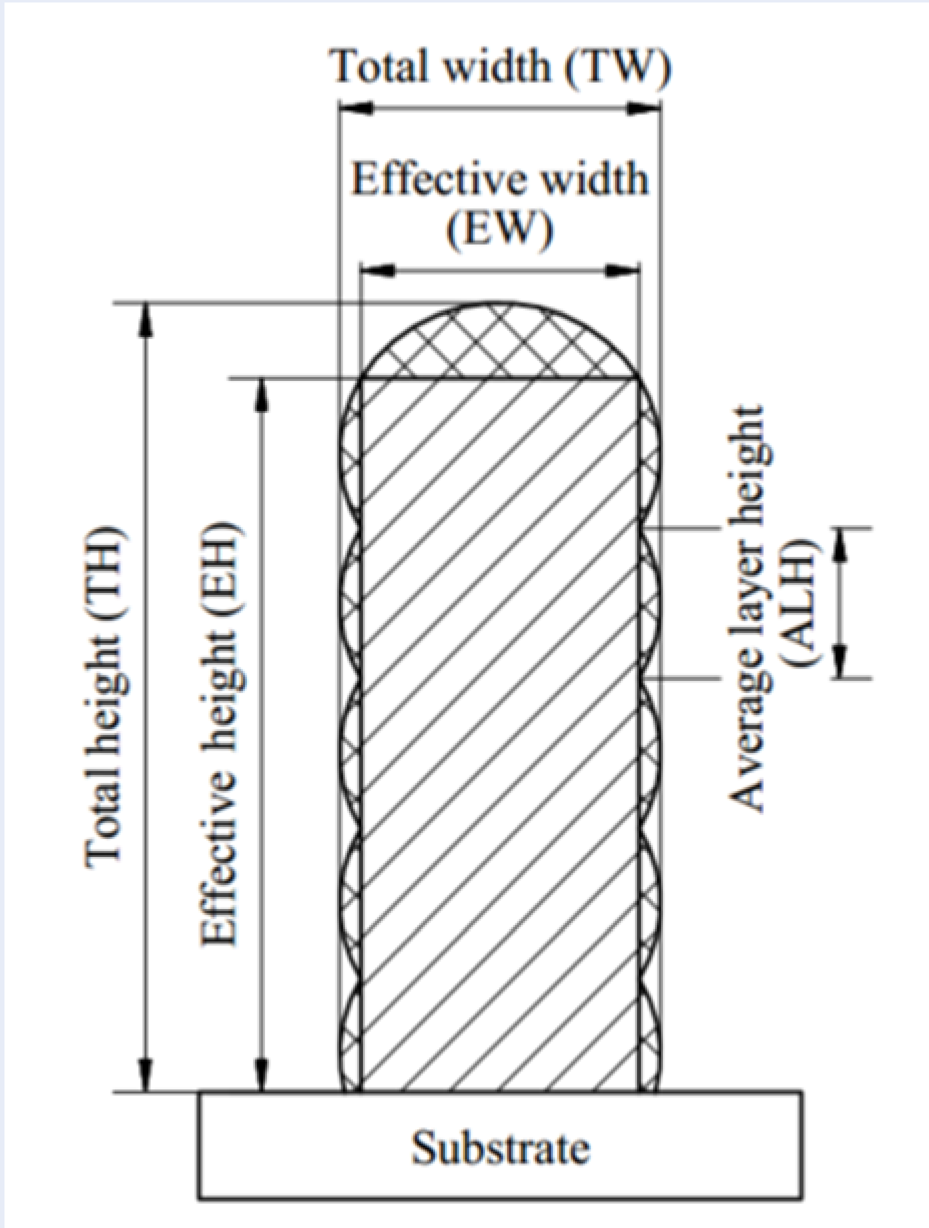

Figure 3: Illustrations of the wall's geometric characteristics

Table 4: Average height value of each layer (ALH)

Sample	v (cm/ph)	TH (mm)	Number of layers	ALH (mm)
No. 1	65	37.30	20	1.87
No. 2	50	40.93	20	2.05
No. 3	35	52.52	20	2.63

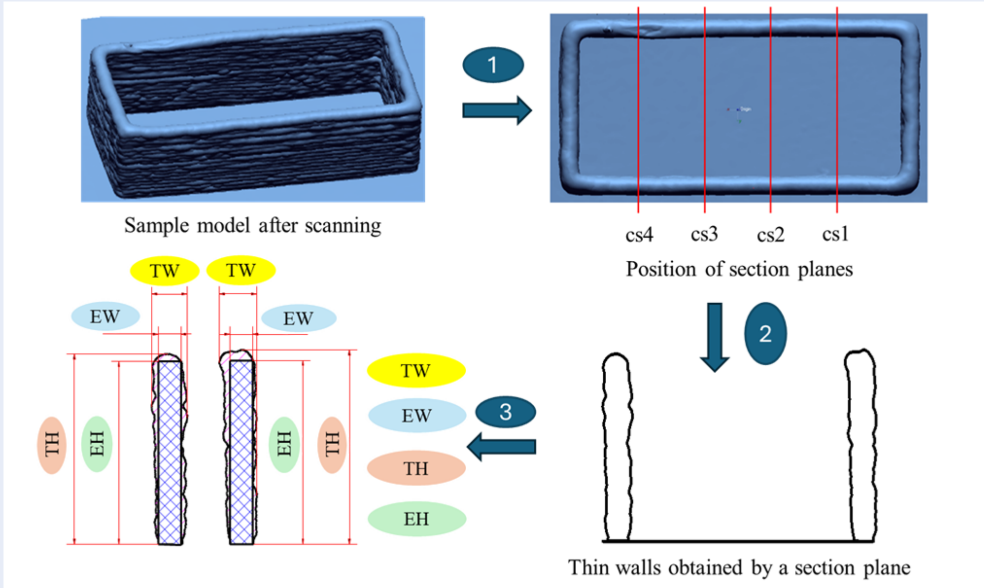

Figure 4: Process of collecting geometric characteristics (dimensions in mm)

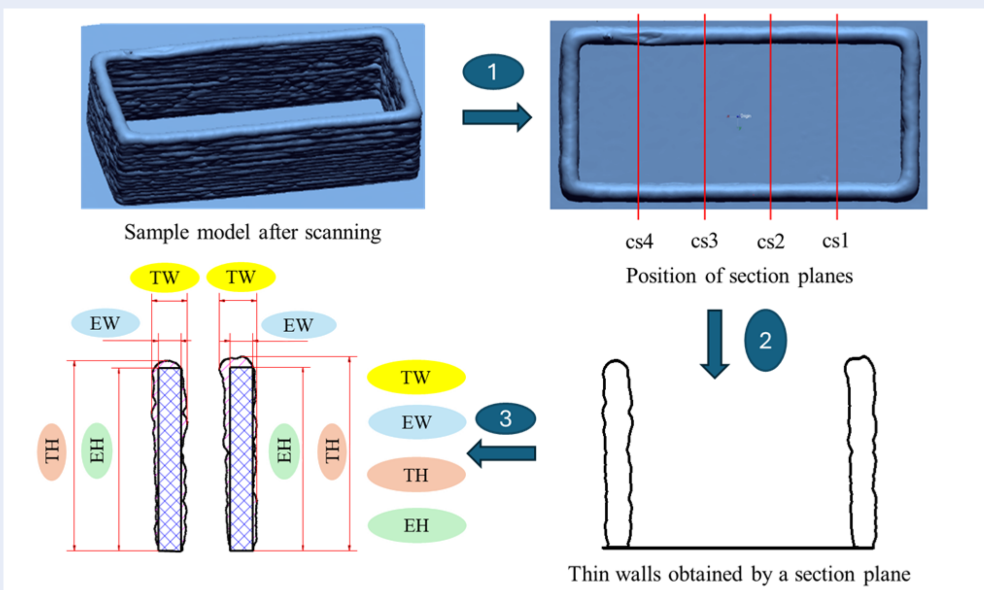

Figure 5: Process of determining the surface roughness

speeds (from 35 to 50 cm/min), whereas it slowly decreases at high values of v, from 50 to 65 cm/min (Figure 6a).

Figure 6b shows that both the values of TW and EW gradually decrease with increasing v. Specifically, the overall width of the wall (TW) is 9.39 mm, 8.00 mm, and 6.83 mm when v is set at 35, 50, and 65 cm/min, respectively. The effective width of each sample (EW) is also proportional to the overall thickness, and its values are 5.9 mm 5.04 mm and 4.3 mm at v = (35, 50, and 65) cm/min, respectively.

Figure 7 illustrates the four surface portions of the thin-walled sample "No. 1" that were extracted from the 3D scanned data through the procedure in Figure 5. These representative surfaces were used to measure surface roughness parameters (S_z, S_a, and S_q) via Omnisurf 3D software. Figure 8 shows the morphology characterization of the surface portion in Figure 7.

The surface roughness parameters of all the samples are shown in Table 5 and Figure 9. The average measurement values are represented to evaluate and compare all the samples.

The maximum roughness S_z value decreases from 168.968 μm to 108.464 μm when v increases from 35 to 50 cm/min, respectively. When v increases from 50 to 65 cm/min, S_z tends to increase from 108.464 μm to 128.811 μm. Similarly, the average roughness S_a and the mean square roughness S_q have similar trends. For example, S_a decreases from 5.902 μm to 4.326 μm when v increases from 35 cm/min to 50 cm/min, whereas it increases from 4.326 μm to 5.394 μm *as v increases* from 50 cm/min to 65 cm/min. S_q decreases from 9.005 μm to 6.544 μm when v increases from 35 cm/min to 50 cm/min, and it increases from 6.544 μm to 8.115 μm *as v increases* from 50 cm/min to 65 cm/min.

DISCUSSION

Effects of *LHI* on *ALH*, *TW*, and *EW*

As mentioned previously, the linear heat input (LHI) plays a crucial role in determining the dimensions and properties of the deposited layers. When the LHI increases, a greater amount of energy is applied to melt the filler wire and the base metal, resulting in larger melting pool dimensions and deeper penetration into the base material. Consequently, increasing LHI tends to result in thicker layers and increased ALH (Figure 11a). Similarly, TW and EW increase with increasing LHI (Figure 11b).

The effect trend of LHI on ALH, TW, and EW is opposite to that of v. Figure 6 shows that all the ALH, TW, and EW values decrease with increasing v. This can be explained by the nature of the process parameters. v indicates the rate at which the amount of molten material is deposited into a welding line, whereas LHI refers to the amount of heat applied per unit length of deposition. As indicated in Eq. (1), the LHI is high at a low value of v [28,29]. At a fixed value of WFS, when the LHI increases (or v decreases), the ability to melt the metal wire is greater, more material is melted and added to the weld pool, and the solidification process also takes longer [19]. Therefore, the melting pool and weld bead become increasingly larger. This is why all the characteristics ALH, TW, and EW increase (Figure 11).

Effects of *LHI* on surface roughness

The influence of LHI on surface roughness parameters is similar to the influence of v, meaning that they decrease when the LHI increases from 191 to 245 J/mm and increase again when the LHI increases from 245 to 352 J/mm (Figure 12). The reason is that when *WFS is maintained*, increasing v reduces the WFS/v ratio, and the staircase effect between layers decreases, leading to a decrease in surface roughness, and the surface quality gradually stabilizes. When v is too low, the amount of heat in the weld pool is large, and the cooling rate is low. After deposition, the surface unevenness and surface roughness are high. As v increases, this heat buildup decreases, the material melts and solidifies more stably, the surface roughness becomes more uniform, and the values decrease [19]. However, if v continues to increase, the stability of the arc gradually deteriorates. This adversely affects the surface roughness. As a result, the surface roughness increases, and the surface quality deteriorates.

CONCLUSIONS

This study investigated the influence of various process parameters, specifically the welding speed v and linear heat input LHI, on the geometric characteristics and material deposition efficiency of the WAAM process for Inconel 625 alloys. The main conclusions are expressed as follows:

- As the welding speed v increases, the LHI and the volume of material added to the melting pool decrease, causing the average layer height, total width, and effective width to decrease.
- The average layer height, total width, and effective width increase when the LHI increases.
- With increasing welding speed v and LHI, the maximum roughness S_z, average roughness S_a, and mean square roughness S_q decrease. They continue to increase as the welding speed v or LHI continues to increase.

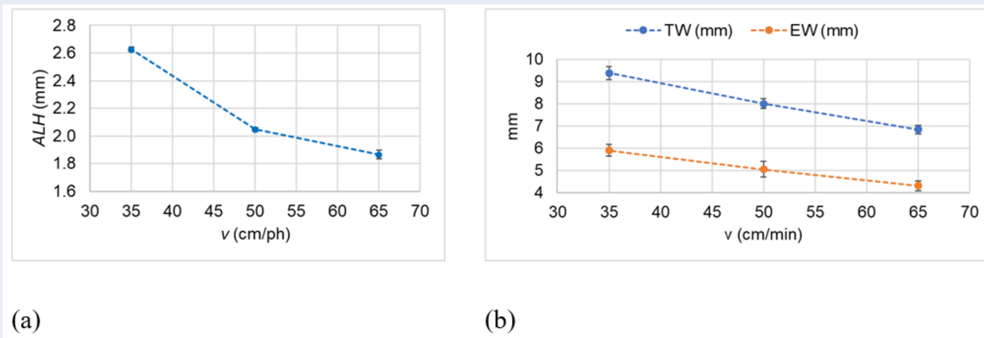

Figure 6: The influence of *v* on (a) *ALH* and (b) *TW* and *EW*

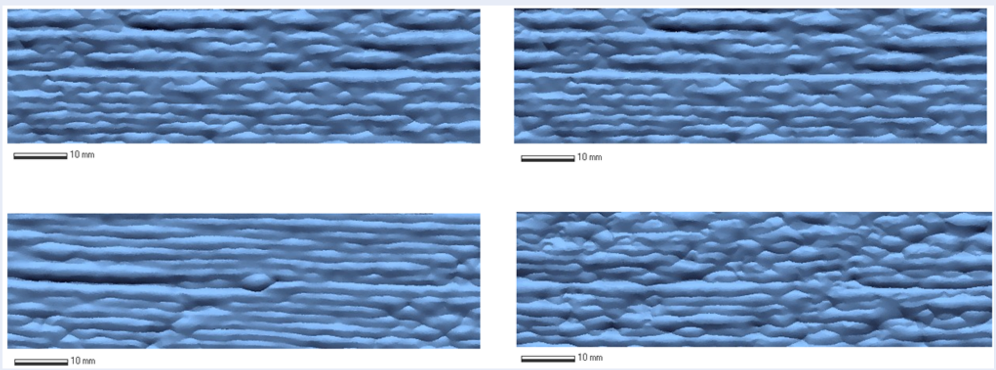

Figure 7: The surface portions of sample No. 1

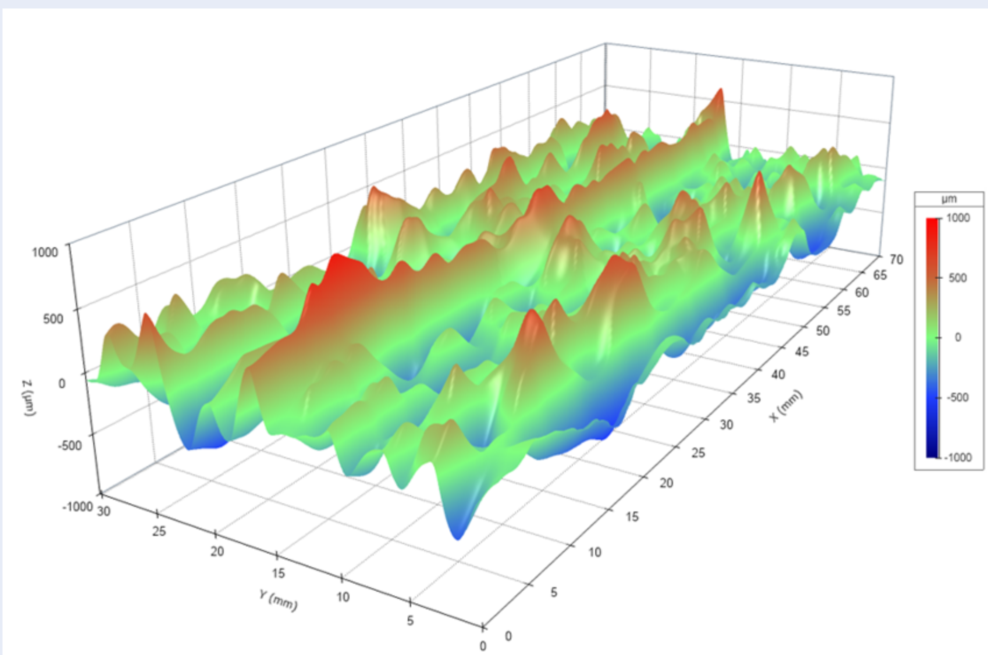

Figure 8: An example of the surface morphology observed in Omnisurf 3D

Table 5: Surface roughness parameters measured via Omnisurf 3D software

Sample	Number of measurements	S_z (μm)	S_a (μm)	S_q (μm)
No. 1	1	96.05	5.29	7.76
	2	129.18	5.41	8.20
	3	156.06	5.04	7.81
	4	133.96	5.84	8.70
	Average	128.811	5.394	8.115
	Standard deviation	± 24.783	± 0.336	± 0.434
No. 2	1	124.912	4.019	6.106
	2	122.316	4.257	6.586
	3	89.041	4.285	6.319
	4	97.586	4.741	7.166
	Average	108.464	4.326	6.544
	Standard deviation	± 17.870	± 0.302	0.459
No. 3	1	194.657	6.235	9.6
	2	169.984	5.775	8.565
	3	157.580	5.562	8.792
	4	153.649	6.034	9.064
	Average	168.968	5.902	9.005
	Standard deviation	18.487	0.294	0.446

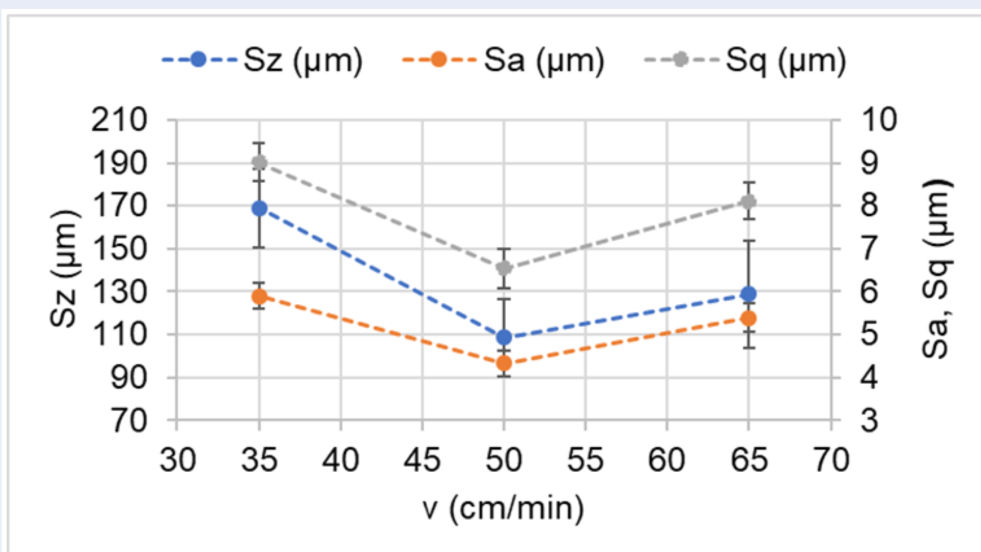

Figure 9: Influence of v on S_z, S_a, and S_q

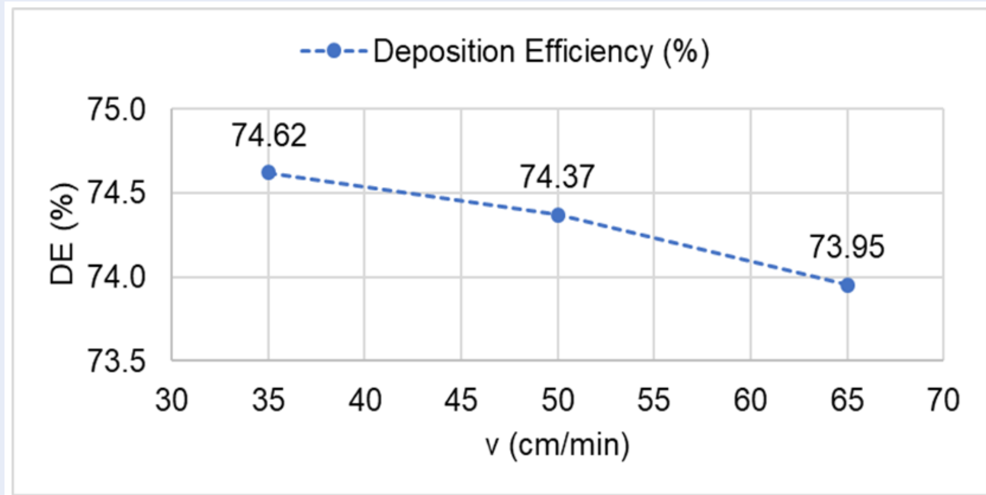

Figure 10: Influence of *v* on *DE*

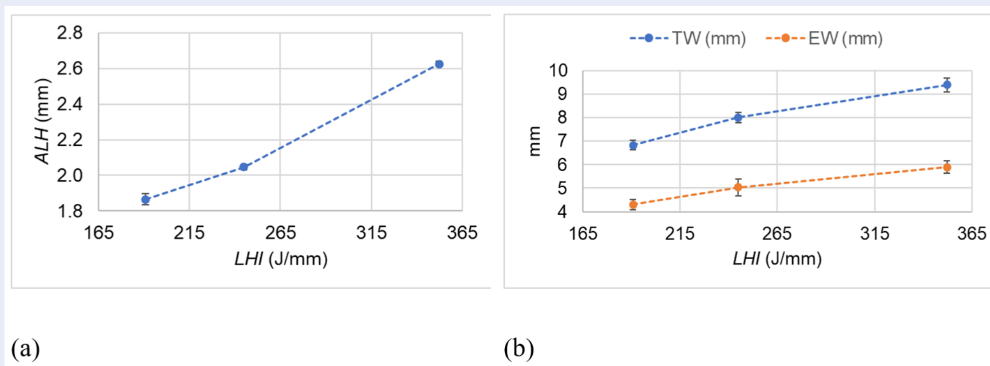

Figure 11: Influence of LHI on (a) ALH and (b) TW and EW

The findings of this study provide insight into the effects of process parameters (v and LHI) on the geometric characteristics of as-built parts, which can support the adjustment of the process parameters in the CMT-WAAM process of Inconel 625 alloy to achieve the expected quality. Additionally, the estimated S_z value can be considered a machining allowance for finishing operations.

In this study, only the effects of the process parameters on the geometric characteristics of the walls were observed. In future works, it will be interesting to develop regression models for all the characteristics with high accuracy. These models can be used to predict the proper parameters and more process parameters to achieve the desired quality. Moreover, it is also important to investigate the microstructures and mechanical properties of the as-built material to confirm its feasibility in real applications.

LIST OF ABBREVIATIONS

GMAW: gas-metal arc welding

AM: Additive Manufacturing

GTAW: gas tungsten arc welding

PAW: Plasma arc welding

MIG: Metal Inerst Gas

TIG: Tungsten Inerts the Gas

CMT: Cold Metal Transfer

LHI: linear heat input

ALH: Average layer height

TW: Total width

EW: Effective Width

TH: Total Height

EH: Effective Height

DE: Deposition efficiency

WFS: Wire Feed Speed

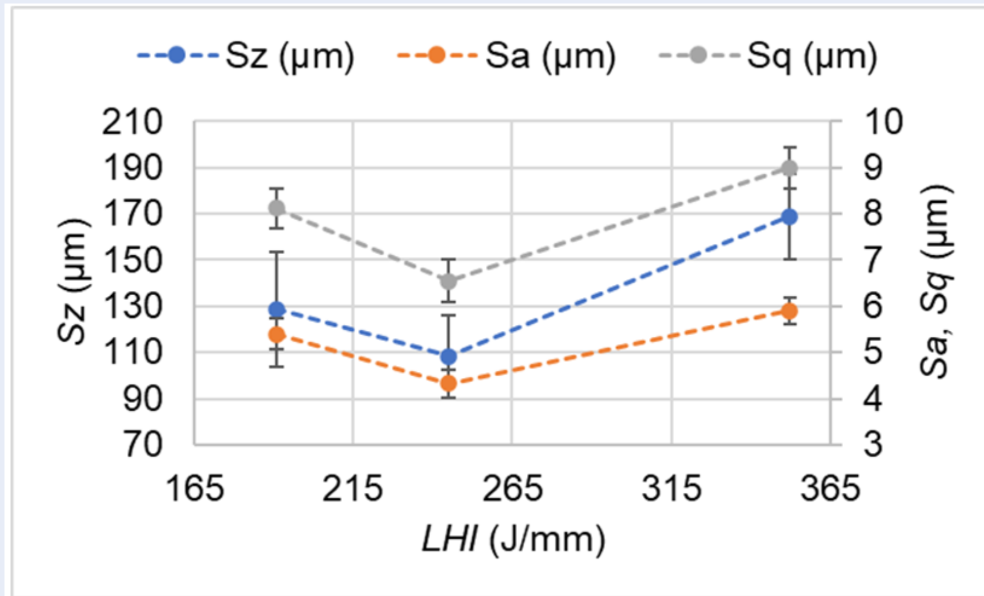

Figure 12: Influence of *LHI* on S_z, S_a, and S_q

ACKNOWLEGEMENTS

This research is funded by the Vietnam National Foundation for Science and Technology Development (NAFOSTED) under grant number 107.99-2023.17.

DATA AVILABILITY

All the data generated or analyzed during this study are included in this published article.

CONFLICT OF INTEREST

The authors declare that they have no competing interests.

REFERENCES

1. Williams SW, Martina F, Addison AC, et al. Wire + Arc Additive Manufacturing. Mater Sci Technol. 2016;32:641-647;Available from: https://doi.org/10.1179/1743284715Y.0000000073.
2. Saleh B, Fathi R, Tian Y, et al. Fundamentals and advances of wire arc additive manufacturing: materials, process parameters, potential applications, and future trends. Springer London; 2023;Available from: https://doi.org/10.1007/s43452-023-00633-7.
3. Tomar B, Shiva S, Nath T. A review on wire arc additive manufacturing: Processing parameters, defects, quality improvement and recent advances. Mater Today Commun. 2022;31:103739;Available from: https://doi.org/10.1016/j.mtcomm.2022.103739.
4. Le VT, Mai DS, Paris H. Influences of the compressed dry air-based active cooling on external and internal qualities of wire-arc additive manufactured thin-walled SS308L components. J Manuf Process. 2021;62:18-27;Available from: https://doi.org/10.1016/j.jmapro.2020.11.046.
5. Guo N, Leu MC. Additive manufacturing: technology, applications and research needs. Front Mech Eng. 2013;8:215-243;Available from: https://doi.org/10.1007/s11465-013-0248-8.
6. Li Z, Cui Y, Wang L, et al. An investigation into Ti-22Al-25Nb in situ fabricated by electron beam freeform fabrication with an innovative twin-wire parallel feeding method. Addit Manuf. 2022;50:102552;Available from: https://doi.org/10.1016/j.addma.2021.102552.
7. Jafari D, Vaneker THJ, Gibson I. Wire and arc additive manufacturing: Opportunities and challenges to control the quality and accuracy of manufactured parts. Mater Des. 2021;202:109471;Available from: https://doi.org/10.1016/j.matdes.2021.109471.
8. Wanwan J, Chaoqun Z, Shuoya J, et al. Wire Arc Additive Manufacturing of Stainless Steels: A Review. Appl Sci (Switzerland). 2020;10:1563;Available from: https://doi.org/10.3390/app10051563.
9. Ding D, Pan Z, Cuiuri D, Li H. Wire-feed additive manufacturing of metal components: technologies, developments and future interests. Int J Adv Manuf Technol. 2015;81:465-481;Available from: https://doi.org/10.1007/s00170-015-7077-3.
10. Horgar A, Fostervoll H, Nyhus B, et al. Additive manufacturing using WAAM with AA5183 wire. J Mater Process Technol. 2018;259:68-74;Available from: https://doi.org/10.1016/j.jmatprotec.2018.04.014.
11. Wu B, Pan Z, Ding D, et al. A review of the wire arc additive manufacturing of metals: properties, defects and quality improvement. J Manuf Process. 2018;35:127-139;Available from: https://doi.org/10.1016/j.jmapro.2018.08.001.
12. Pant H, Arora A, Gopakumar GS, et al. Applications of wire arc additive manufacturing (WAAM) for aerospace component manufacturing. Int J Adv Manuf Technol. 2023;127:4995-5011;Available from: https://doi.org/10.1007/s00170-023-11623-7.
13. Ridings A, Pan A, Yin H, et al. A Literature Review of WAAM and Future Application in Buildings. In: In Commons. ACSA Press; 2023. p. 54-61;Available from: https://doi.org/10.35483/ACSA.AM.111.8.
14. Wang Z, Guan K, Gao M, et al. The microstructure and mechanical properties of deposited-IN718 by selective laser melting. J Alloys Compd. 2012;513:518-523;Available from: https://doi.

org/10.1016/j.jallcom.2011.10.107.
15. Amudha A, Shashikala HD, Nagaraja HS. Corrosion protection of low-cost carbon steel with SS-309Mo and Inconel-625 bimetallic weld overlay. Mater Res Express. 2019;6:046523;Available from: https://doi.org/10.1088/2053-1591/aafba6.
16. Dinda GP, Dasgupta AK, Mazumder J. Laser aided direct metal deposition of Inconel 625 superalloy: Microstructural evolution and thermal stability. Mater Sci Eng A. 2009;509:98-104;Available from: https://doi.org/10.1016/j.msea.2009.01.009.
17. Li S, Wei Q, Shi Y, et al. Microstructure Characteristics of Inconel 625 Superalloy Manufactured by Selective Laser Melting. J Mater Sci Technol. 2015;31:946-952;Available from: https://doi.org/10.1016/j.jmst.2014.09.020.
18. Dinovitzer M, Chen X, Laliberte J, et al. Effect of wire and arc additive manufacturing (WAAM) process parameters on bead geometry and microstructure. Addit Manuf. 2019;26:138-146;Available from: https://doi.org/10.1016/j.addma.2018.12.013.
19. Xiong J, Li Y, Li R, Yin Z. Influences of process parameters on surface roughness of multilayer single-pass thin-walled parts in GMAW-based additive manufacturing. J Mater Process Technol. 2018;252:128-136;Available from: https://doi.org/10.1016/j.jmatprotec.2017.09.020.
20. Xu FJ, Lv YH, Xu BS, et al. Effect of deposition strategy on the microstructure and mechanical properties of Inconel 625 superalloy fabricated by pulsed plasma arc deposition. Mater Des. 2013;45:446-455;Available from: https://doi.org/10.1016/j.matdes.2012.07.013.
21. Cheepu M, Lee CI, Cho SM. Microstructural Characteristics of Wire Arc Additive Manufacturing with Inconel 625 by Super-TIG Welding. Trans Indian Inst Met. 2020;73:1475-1479;Available from: https://doi.org/10.1007/s12666-020-01915-x.
22. Kumar A, Maji K, Shrivastava A. Investigations on Deposition Geometry and Mechanical Properties of Wire Arc Additive Manufactured Inconel 625. Int J Precis Eng Manuf. 2023;Available from: https://doi.org/10.1007/s12541-023-00827-2.
23. Motwani A, Kumar A, Talekar A, Puri Y. Process parameters optimization for cold metal transfer-deposited IN625 single-layer bead features by entropy weightage-assisted gray-based Taguchi analysis. Proc Inst Mech Eng Part E J Process Mech Eng. 2023;Available from: https://doi.org/10.1177/09544089221150196.
24. Babu SDD, Sevvel P, Kumar RS. Simulation of heat transfer and analysis of impact of tool pin geometry and tool speed during friction stir welding of AZ80A Mg alloy plates. J Mech Sci Technol. 2020;34:4239-4250;Available from: https://doi.org/10.1007/s12206-020-0916-7.
25. Selvi S, Vishvaksenan A, Rajasekar E. Cold metal transfer (CMT) technology - An overview. Def Technol. 2018;14:28-44;Available from: https://doi.org/10.1016/j.dt.2017.08.002.
26. Belhadj M, Kromer R, Werda S, Darnis P. Effect of cold metal transfer-based wire arc additive manufacturing parameters on geometry and machining allowance. Int J Adv Manuf Technol. 2024;131:739-748;.
27. Girinath B, Shanmugam NS, Sathiyanarayanan C. Studies on influence of torch orientation on microstructure, mechanical properties and formability of AA5052 CMT welded blanks. Arch Civ Mech Eng. 2020;20:15;Available from: https://doi.org/10.1007/s43452-020-00021-5.
28. Le VT, Mai DS, Bui MC, et al. Influences of the process parameter and thermal cycles on the quality of 308 L stainless steel walls produced by additive manufacturing utilizing an arc welding source. Weld World. 2022;66:1565-1580;Available from: https://doi.org/10.1007/s40194-022-01330-4.
29. Le VT, Bui MC, Nguyen TD, et al. On the connection of the heat input to the forming quality in wire-and-arc additive manufacturing of stainless steels. Vacuum. 2023;209:111807;Available from: https://doi.org/10.1016/j.vacuum.2023.111807.